



# Ionic liquid-induced strategy for carbon quantum dots/BiOX (X = Br, Cl) hybrid nanosheets with superior visible light-driven photocatalysis

Jiexiang Xia<sup>a,1</sup>, Jun Di<sup>a,1</sup>, Haitao Li<sup>c</sup>, Hui Xu<sup>a</sup>, Huaming Li<sup>a,\*</sup>, Shaojun Guo<sup>b,\*</sup>

<sup>a</sup> School of Chemistry and Chemical Engineering, Institute for Energy Research, Jiangsu University, 301 Xuefu Road, Zhenjiang 212013, PR China

<sup>b</sup> College of Engineering, Peking University, Beijing 100871, PR China

<sup>c</sup> ARC Centre for Electromaterials Science, School of Chemistry, Monash University, Clayton, Victoria 3800, Australia

## ARTICLE INFO

### Article history:

Received 18 March 2015

Received in revised form 25 June 2015

Accepted 21 July 2015

Available online 26 July 2015

### Keywords:

BiOX nanosheets

Carbon quantum dots

Ionic liquids

Photocatalysis

Visible light irradiation

## ABSTRACT

A novel one-step ionic liquid induced strategy has been reported for the controlled synthesis of carbon quantum dots (CQDs)/BiOX (X = Br, Cl) hybrid nanosheets with tunable CQDs loading contents. Such synthetic process allows the CQDs well dispersed on the surface of BiOX nanosheets. Three different types of pollutants, such as phenol rhodamine B (RhB), antibacterial agent ciprofloxacin (CIP) and endocrine disrupting chemical bisphenol A (BPA) were chosen to evaluate the photocatalytic activity of CQDs/BiOX composite nanosheets. They show very interesting CQDs loading content and X composition-dependent photocatalytic activity with 3 wt% CQDs/BiOBr nanosheets showing the highest photocatalytic activity (much better than pure BiOBr nanosheets) for the degradation of RhB, CIP and BPA under visible light irradiation. The results reveal that there are three factors in promoting the photocatalysis of 3 wt% CQD/BiOBr nanosheets: high visible light absorbance, high separation efficiency of photo-induced electrons and holes and lower resistance. The active species trap experiments and electron spin resonance (ESR) reveal that during the photocatalytic process, hole and  $O_2^{\cdot-}$  become the dominant species for the degradation of pollutants. The unique strategy demonstrated here can be extended to other hybrid nanosheet systems, making it possible to design and tune advanced photocatalysts for other important chemical and catalytic reactions.

© 2015 Elsevier B.V. All rights reserved.

## 1. Introduction

Two-dimensional (2D) layered nanosheets (e.g. graphene, hexagonal boron nitride, dichalcogenide and graphitic carbon nitride) have grown extensively research interest due to their immense technological promise and potential applications in electronics, catalysis and energy storage [1–4]. They show many new and enhanced promising properties, which can be not achieved by their bulk counterparts [5–8]. Bismuth oxyhalide, BiOX (X = Cl, Br), an important V–VI–VII ternary compound, crystallizing in the structure of tetragonal matlockite, is one of a new class of 2D layered materials for photocatalytic energy conversion and environment remediation [9–12]. They show the good chemical stability and capability of degrading toxic organic pollutants in water under

visible light irradiation [13–17]. However, at the present stage, the photocatalytic performance of individual 2D BiOX materials is still limited by their low efficiency of light absorption, slow rate of charge transfer and high recombination probability of the photo-generated electron–hole pairs. In this regards, the rational design of new 2D BiOX nanosheets-based hybrids integrating another functional component with high conductivity and excellent absorption ability located at other ranges of solar spectrum is highly desirable, yet a great challenge.

Carbon quantum dots (CQDs), known as a novel class of recently discovered carbon-based materials, exhibit the excellent photo-induced electron transfer, electron reservoir properties and good up-converted photoluminescence behavior, which open a new way for efficiently utilizing the full spectrum of sunlight [18–21]. Therefore, the remarkable properties of individual 2D BiOX layered materials, ionic liquids and CQDs [22–26], motivate us whether we can rationally design a new class of CQDs/BiOX hybrid nanosheets with much stronger and wider absorption properties for more efficient photocatalysts. However, it is still a great challenge for the

\* Corresponding author.

E-mail addresses: [lh@ujs.edu.cn](mailto:lh@ujs.edu.cn) (H. Li), [sjguo@coe.pku.edu.cn](mailto:sjguo@coe.pku.edu.cn) (S. Guo).

<sup>1</sup> These authors contributed equally to this work.

synthesis of such interesting CQDs/BiOX hybrid nanosheets with tunable CQDs loading amount for maximizing the photocatalytic performance.

Herein, we demonstrate one-pot ionic liquid induced hydrothermal strategy for the in situ synthesis of 2D CQDs/BiOX hybrid nanosheets with tunable CQDs loading amount for enhancing the photocatalytic degradation of phenol rhodamine B (RhB), antibacterial agent ciprofloxacin (CIP) and endocrine disrupting chemical bisphenol A (BPA). Ionic liquid acts as both solvent and dispersing agent, which is beneficial for the uniform dispersion of CQDs on the surface of BiOX nanosheets. Simultaneously, ionic liquid based on 1-alkyl-3-methylimidazolium cations can show the aggregation behavior and form micelles in solution. This also makes it work as soft template and reactant, which play a crucial role on the shape control of the 2D thin BiOX nanosheets. We think that such CQDs/BiOX hybrid nanosheets are particularly unique for visible light-driven photocatalysis. The photocatalytic activities of CQDs/BiOX hybrid nanosheets were evaluated by the degradation of RhB, CIP, and BPA under visible light irradiation. We found that CQDs/BiOX hybrid materials showed much higher photocatalytic activity for the degradation of above three pollutants than individual BiOX, highlight the important role of CQDs in enhancing the photocatalytic activity. In all the investigated CQDs/BiOX hybrid materials with different CQD loading amounts, the 3 wt% CQDs/BiOBr nanosheets are the most active photocatalyst. The results from photocatalytic experiments, diffuse reflectance spectroscopy, photocurrent and electrochemical impedance spectroscopy (EIS) analysis reveal that such photocatalysis enhancement of CQDs/BiOBr can be ascribed to the high light absorbance and high separation efficiency of the photogenerated electron–holes pairs induced by CQDs. Most notably, herein our electron spin resonance (ESR) results reveal that during the photocatalytic process,  $O_2^{\bullet-}$  is produced on CQDs/BiOBr nanosheets and become the dominant species for the degradation of pollutants.

## 2. Experimental

### 2.1. Material and sample preparation

All chemicals were analytical grade and used without further purification. Phenol rhodamine B (RhB), antibacterial agent ciprofloxacin (CIP) and endocrine disrupting chemical bisphenol A (BPA) were purchased from Sinopharm and used without further treatment. The ionic liquid  $[C_{16}mim]Br$  (1-hexadecyl-3-methylimidazolium bromide) (99%) and  $[C_{16}mim]Cl$  (1-hexadecyl-3-methylimidazolium chloride) (99%) were purchased from Shanghai Chengjie Chemical Co. Ltd. The carbon quantum dots (CQDs) dispersed in water solution was prepared through the previous protocol [27]. The CQDs solids were obtained through the freeze-drying of the CQDs solution. DMPO (Sigma Chemical Co.)

### 2.2. Fabrication of CQDs/BiOX composite nanosheets

In a typical synthesis of CQDs/BiOBr composite, 1 mmol ionic liquid  $[C_{16}mim]Br$  and 1 mmol  $Bi(NO_3)_3 \cdot 5H_2O$  were dissolved into 20 mL deionized water containing a certain amount of CQDs. Then, the pH value of the solution was adjusted to 1 by adding nitric acid. The mixture was further stirred for 0.5 h at room temperature in air, and transferred into 25 mL Teflon-lined autoclave. The autoclave was then heated at 140 °C for 24 h under autogenous pressure and cooled down to room temperature. The obtained samples were centrifuged and washed with distilled water and ethanol for three times. Finally, the samples were dried in a vacuum at 50 °C for 24 h before further characterization. The added contents of CQDs in the CQDs/BiOBr hybrid nanosheets were controlled to 0.5 wt%, 1 wt%,

3 wt% and 5 wt%, respectively, by simply controlling the weight ratio of CQDs to BiOBr.

The CQDs/BiOCl composites were also prepared by a similar method by using  $[C_{16}mim]Cl$  instead of  $[C_{16}mim]Br$ . The weight contents of CQDs in the CQDs/BiOCl composites were 1 wt%, 3 wt% and 5 wt%, respectively.

### 2.3. Characterization

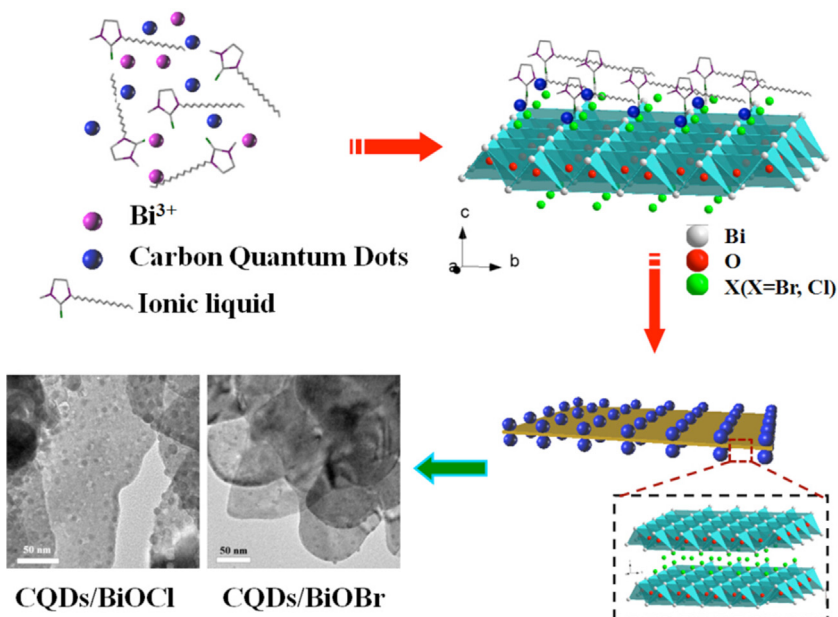
The powder X-ray diffraction (XRD) pattern was performed on a Bruker D8 diffractometer equipped with Cu-K $\alpha$  radiation. X-ray photoelectron spectroscopy (XPS) was measured on a PHI5300 with a monochromatic Mg K $\alpha$  source to test the elements on the surface of nanosheets. FT-IR spectrum was performed on a Nicolet FT-IR spectrophotometer (Nexus 470, Thermo Electron Corporation) using KBr disk as the reference at room temperature. The field-emission scanning electron microscopy (FE-SEM) measurements were carried out with a field-emission scanning electron microscope (JEOL JSM-7001F) equipped with an energy-dispersive X-ray spectroscopy (EDS) operated at an acceleration voltage of 10 kV. Transmission electron microscopy (TEM) images were taken with a JEOL-JEM-2010 (JEOL, Japan) operating at 200 kV. UV–vis diffuse reflectance spectroscopy were recorded on an UV-2450 spectrophotometer (Shimadzu Corporation, Japan) using  $BaSO_4$  as the reference. The photocurrent and electrochemical impedance spectroscopy (EIS) were measured with an electrochemical analyzer (CHI 660B Chenhua Instrument Company). The high performance liquid chromatography (HPLC) setup was equipped with two Varian ProStar210 pumps, an Agilent TC-C (18) column and a Varian ProStar325 UV–vis Detector at 230 nm. A solution of methanol and  $H_2O$  in the ratio of 75:25 (v/v) was used as the mobile phase at the rate of 1 mL/min. 20  $\mu$ L of the sample solution was injected. The electron spin resonance (ESR) signals of radicals spin-trapped were examined on a Bruker model ESR JES-FA200 spectrometer by spin-trap reagent DMPO in water and methanol.

### 2.4. Photocatalytic activity measurement

To compare the photocatalytic activity of pure BiOX and CQDs/BiOX composites with different contents, a series of photodegradation experiments were carried out by using RhB, CIP and BPA as target pollutants under the visible-light irradiation. A 300 W Xe lamp with a 400 nm cutoff filter was used as the light source. Experiments were carried out in a Pyrex photocatalytic reactor with a circulating water system to prevent thermal catalytic effects. In a typical photocatalytic experiment, 0.02 g, 0.03 g and 0.05 g of samples were dispersed into 100 mL of RhB ( $10 \text{ mg L}^{-1}$ ) solutions, 100 mL of CIP ( $10 \text{ mg L}^{-1}$ ) solutions and 100 mL of BPA ( $10 \text{ mg L}^{-1}$ ) solutions, respectively. Prior to the irradiation, the suspensions were magnetically stirred for 30 min in the dark to achieve a saturated RhB, CIP or BPA absorption onto the photocatalyst surface. During every irradiation interval, 3 mL suspension was collected and centrifuged (13,000 rpm, 3 min) to remove the photocatalyst. The RhB and CIP concentrations were analyzed with a UV–vis spectrophotometer (UV-2450, Shimadzu) at the absorption wavelength of 553 nm and 276 nm, respectively. HPLC was used to analyze the concentration of BPA.

### 2.5. Photoelectrochemical measurements

To investigate the photoelectrochemical (PEC) properties, the BiOBr and CQDs/BiOBr nanosheets modified electrodes were prepared by the following procedures. First, the indium tin oxide (ITO) glass was cut into 3 cm  $\times$  1 cm slices and successively bathed in 1 M NaOH water solution for 10 min and acetone for 30 min, then washed with water and dried prior to use. 2 mg of the as-prepared



**Scheme 1.** Schematic illustration on the synthetic process for CQDs/BiOX hybrid nanosheets.

sample was dispersed in 0.2 mL ethanol and 0.2 mL ethylene glycol (EG) to produce a suspension. 20  $\mu\text{L}$  of the resulting colloidal dispersion was drop-cast onto a piece of ITO slice with a fixed area of  $0.5\text{ cm}^2$  and dried in air at room temperature to form BiOBr and CQDs/BiOBr modified ITO electrodes. All the PEC measurements were performed at a constant potential of 0.2 V (vs. saturated Ag/AgCl). Phosphate buffer solution (PBS, 0.1 M, pH 7.0) was used as the supporting electrolyte throughout the PEC measurements. The PEC and EIS measurement were performed on a CHI660B electrochemical workstation in a standard three-electrode system with a Pt wire as a counter electrode, a saturated Ag/AgCl as a reference electrode and ITO as working electrode. A 500W Xe lamp was utilized as the light source for the PEC measurement. The Nyquist plots were recorded from 100 MHz to 100 kHz frequency range in a 0.1 M KCl solution containing 5 mM  $\text{Fe}(\text{CN})_6^{3-}/\text{Fe}(\text{CN})_6^{4-}$ .

### 3. Results and discussion

#### 3.1. Morphology and structural information

The design and preparation process of CQDs/BiOX hybrid nanosheets is shown in Scheme 1. In a typical process, CQDs with carboxyl groups (proved by Fourier Infrared spectroscopy (Fig. S1a) and X-ray diffraction (XRD, Fig. S1b) with the size of 5 nm (Fig. S1c) were first synthesized from citric acid by a hydrothermal process [27]. They show the strong photoluminescence under ultraviolet irradiation (the inset of Fig. S1c) and also exhibit the typical excitation-dependent PL behavior (Fig. S1d). Then, the CQDs interact with ionic liquid  $[\text{C}_{16}\text{mim}]\text{X}$  by hydrogen bond in water solution. Such interesting hydrogen-bond and self-assembly effect of  $[\text{C}_{16}\text{mim}]\text{X}$  ionic liquid are helpful to control the growth rates of BiOX crystal and allow the crystal to undergo the self-organization into sheet-like structure with the CQDs well dispersed on its surface. The color of the composites is darker with the content of CQDs increasing, confirming the formation of CQDs/BiOX composites (Fig. S2). It should be noted that the present method is not suitable for the synthesis of CQDs/BiOI composites because I ion is easily oxidized to  $\text{I}_2$  during the hydrothermal process.

The morphology of the CQDs/BiOX hybrid nanosheets was examined by scanning electron microscopy (SEM) and transmission

electron microscopy (TEM). Fig. 1a shows the typical SEM image of the 3 wt% CQDs/BiOBr composite nanosheets, showing they have an average size of about  $150\text{ nm} \times 150\text{ nm}$ . The average thickness of CQDs/BiOBr nanosheets is determined to be about 25 nm (Fig. 1a). TEM image (Fig. 1b) of the CQDs/BiOBr nanosheets reveals that numerous CQDs with the size of about 5 nm are uniformly dispersed on the surface of BiOX nanosheets. The formation of CQDs/BiOBr composite nanosheets was further proved by high-resolution TEM (HRTEM) (Fig. 1c). Two distinct lattice spacings in the CQDs/BiOBr are observed. The lattice fringe spacings of 0.332 nm and 0.277 nm correspond to the (002) crystal plane of CQDs and (110) crystallographic planes of BiOBr (JCPDS 73-2061), respectively. Compared with the 3 wt% CQDs/BiOBr nanosheets, the 3 wt% CQDs/BiOCl has a relatively larger size of  $300\text{ nm} \times 300\text{ nm}$  (Figs. 1d and e) and a thickness of about 50 nm. Similarly, the lattice fringe spacings of 0.332 nm and 0.275 nm observed in CQDs/BiOCl correspond to the (002) crystal plane of CQDs and the (110) crystal plane of BiOCl (JCPDS 73-2060) (Fig. 1f) [28]. The above results strongly prove that the CQDs are successfully loaded on the surface of BiOX nanosheets. Based on the elemental mapping images, it can be seen that the C, O, Cl, and Bi elementals are evenly distributed in the CQDs/BiOCl materials (Fig. S3). Similarly, the C, O, Br, and Bi elementals are evenly distributed in the CQDs/BiOBr materials (Fig. S4). We found that without the introduction of any CQDs in the synthesis of CQDs/BiOX, only individual BiOX nanosheets can be prepared (Fig. S5). These BiOX nanosheets with the same thickness as CQDs/BiOX have been used as a control to reveal the more obvious advantage of the as-prepared CQDs/BiOX nanosheets in photocatalysis.

X-ray diffraction (XRD) (Fig. 2) was performed to show the purity and crystallinity of as-prepared CQDs/BiOBr and CQDs/BiOCl with different CQDs contents. The positions of all peaks can be indexed to the tetragonal BiOBr (Fig. 2a, JCPDS No. 73-2061) or tetragonal BiOCl (Fig. 2b, JCPDS No. 73-2060). The characteristic peak for CQDs at  $26^\circ$  is too weak to be observed. No extra characteristic peaks are observed, indicating that there are no impurities in as-prepared hybrid nanosheets. Energy dispersed spectroscopy (EDS) (Fig. S6) of the CQDs/BiOX nanosheets indicate they contain C, O, X, and Bi element. The elements of Bi, O and X come from the BiOX, and the C is from the CQDs. X-ray photoelectron spectroscopy (XPS) was used to investigate the

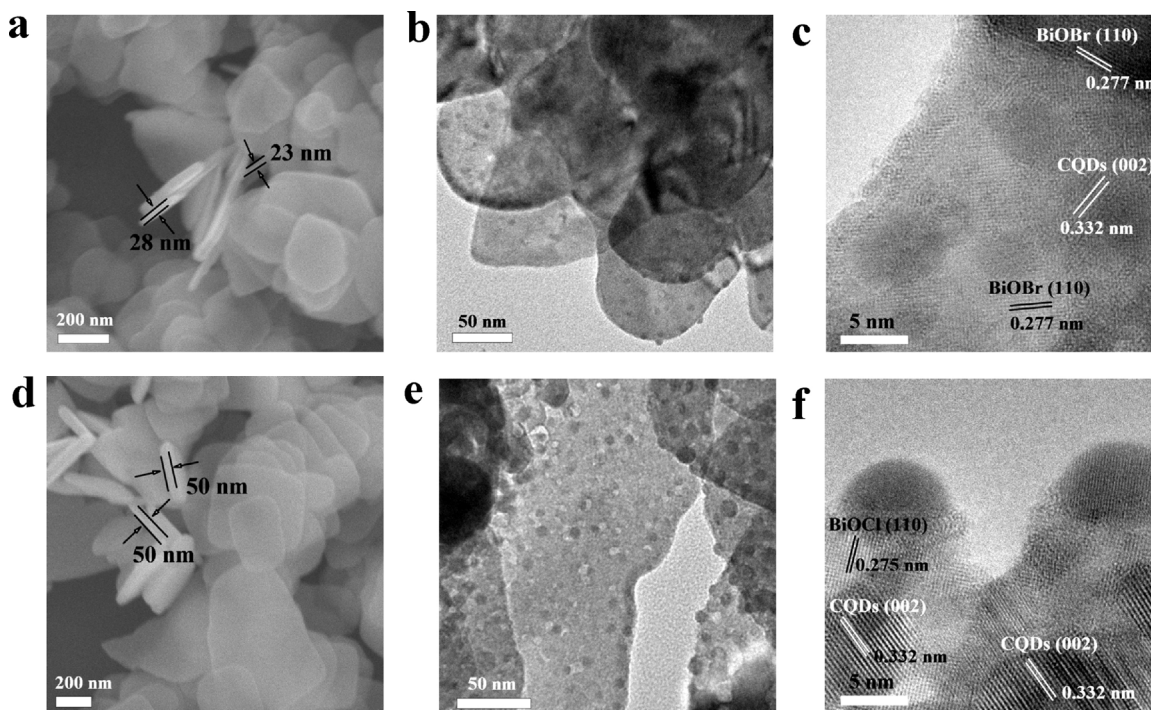


Fig. 1. SEM and TEM images of (a–c) 3 wt% CQDs/BiOBr nanosheets and (d–f) 3 wt% CQDs/BiOCl nanosheets.

surface composition and chemical states in the CQDs/BiOX hybrid nanosheets.

The survey XPS spectra of the CQDs/BiOX nanosheets show that they consist of the elements of Bi, O, X and C (Fig. 3a and b). The high-resolution XPS spectra (Fig. 3c) reveal that the binding energies of Bi 4f<sub>7/2</sub> and Bi 4f<sub>5/2</sub> are located at 158.9 eV and 164.3 eV, respectively, suggesting that Bi<sup>3+</sup> exists in the CQDs/BiOX composites. The binding energy of 529.7 eV associated with O 1s peaks (Fig. 3d), and the binding energies of 284.7 eV, 286.1 eV and 287.3 eV associated with C 1s peaks (the C–C bond with sp<sup>2</sup> orbital, the oxygenated carbon and nitrous carbon, respectively) are observed (Fig. 3e and f), indicating the formation of CQDs [27]. The binding energies of 68.5 eV and 197.7 eV associated with Br<sup>−</sup> and Cl<sup>−</sup> in the CQDs/BiOBr and CQDs/BiOCl composite, respectively (Fig. 3g and h).

Fig. 4 shows the FT-IR spectra of BiOX and CQDs/BiOX hybrid nanosheets with different CQDs loading amounts. The peak at 1460 cm<sup>−1</sup> is attributed to the absorption peaks of –COO<sup>−</sup> [29] whereas the peak at 1598 cm<sup>−1</sup> is associated with the C=O

stretching vibration [30]. These reveal that there are –COOH groups on the surface of the CQDs. The peak at 525 cm<sup>−1</sup> is associated with the Bi–O stretching mode. No characteristic absorption peaks of the ionic liquid are found in the FT-IR spectra, revealing that the ionic liquid can be easily removed from the surface of the photocatalyst by washing with water and alcohol. In the Raman analysis (Figs. S7 and S8), the D band and G band can be found in CQDs/BiOCl and CQDs/BiOBr materials. However, due to the strong fluorescence of CQDs, there have background interference in the CQDs/BiOCl and CQDs/BiOBr materials.

### 3.2. The role of ionic liquids

Inorganic salts have also been used as the control to better understand the role of ionic liquids on the BiOX morphology change. The XRD analysis of CQDs/BiOX nanoplates which prepared via inorganic salts of NaX were provided (Fig. S9). Fig. 5 shows the SEM and TEM images of the BiOX nanoplates, prepared by the use of

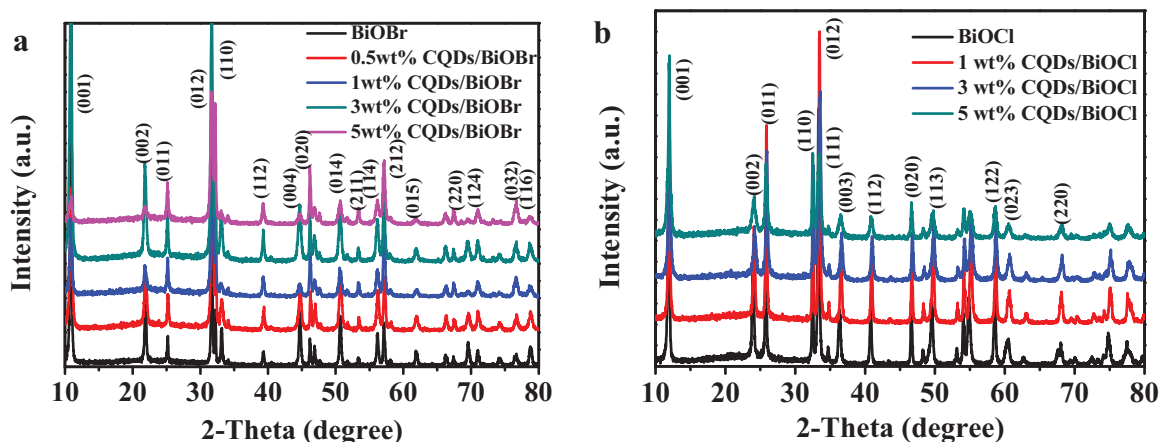
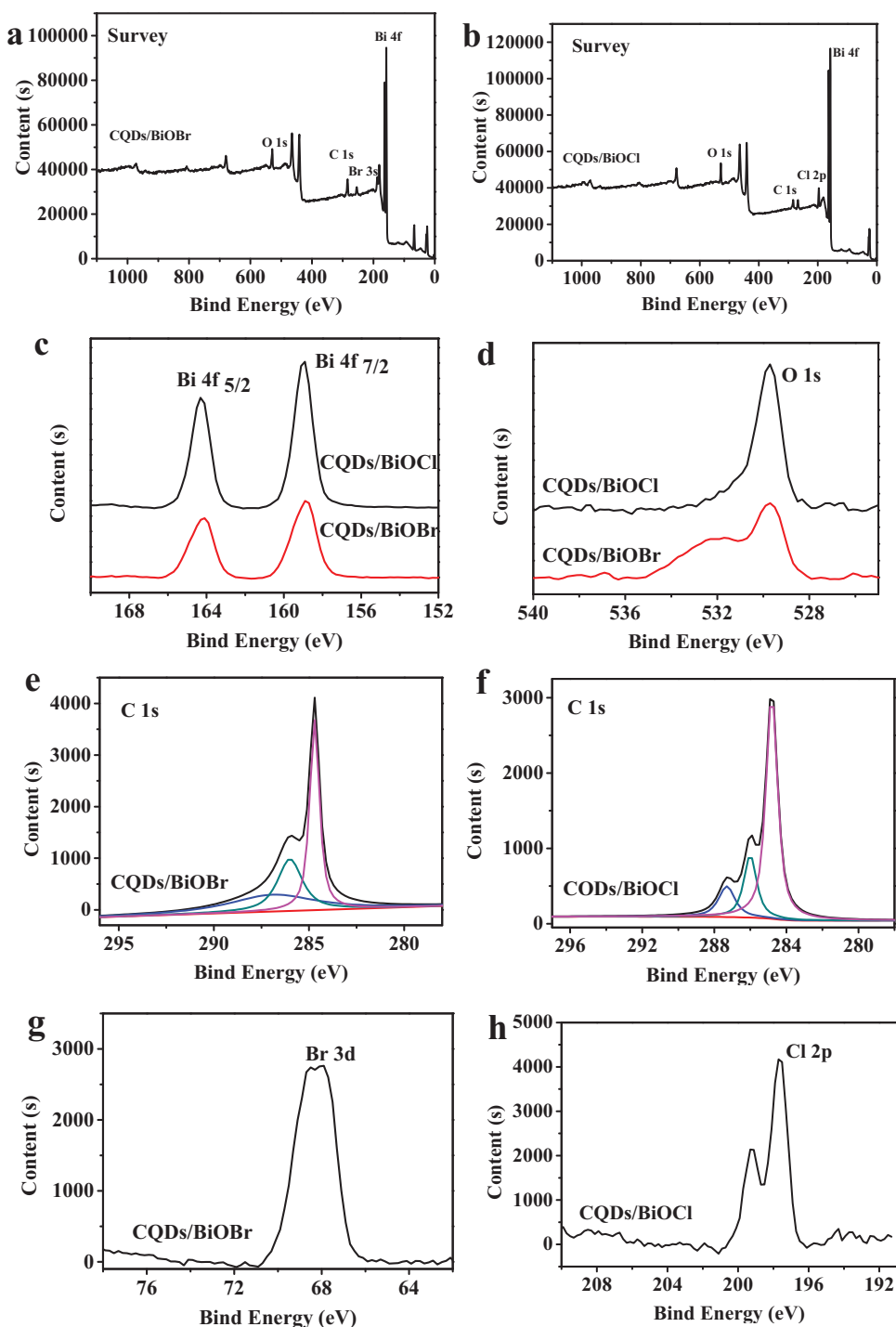


Fig. 2. XRD patterns of the as-prepared (a) CQDs/BiOBr and (b) CQDs/BiOCl with different CQDs loading amount.



**Fig. 3.** XPS spectra of CQDs/BiOBr and (b) CQDs/BiOCl nanosheets. (c) Bi 4f; (d) O 1s; (e) C 1s of CQDs/BiOBr nanosheets; (f) C 1s of CQDs/BiOCl nanosheets; (g) Br 3d of CQDs/BiOBr nanosheets and (h) Cl 2p of CQDs/BiOCl composites.

NaX (X = Br, Cl). The thickness of BiOBr and BiOCl nanoplates were about 100 nm and 400 nm, respectively, much thicker than those of CQDs/BiOBr and CQDs/BiOCl nanosheets prepared by the use of ionic liquid. This phenomenon can be attributed to the strong control ability of the ionic liquids for BiOX nanosheets. As is known, BiOX crystal consists of alternative  $\text{Bi}_2\text{O}_2$  tetrahedrons connected with halogen along the c-axis. When ionic liquid  $[\text{C}_{16}\text{mim}]\text{X}$  was introduced, the hydrogen bonds were formed between the hydrogen atoms at the position 2 in the imidazolium ring and the halogen atoms from BiOX tetrahedrons on the (001) plane. With the

formation of hydrogen bond,  $[\text{C}_{16}\text{mim}]^+$  can be aligned along the c axis of BiOX [31]. Meanwhile, a stabilized self-assembly interaction between the imidazolium rings of the adsorbed  $[\text{C}_{16}\text{mim}]^+$  can reduce the growth rate of the (001) plane in comparison to other crystal plane, and thus induce the preferential growth of BiOX to form uniform sheet-like structure. Meanwhile, the Coulomb force is another important noncovalent interaction in the ionic liquids structure, which could combine with the hydrogen bonds formed between the hydrogen atoms at the position 2 in the imidazolium ring of ionic liquids and act on the surface

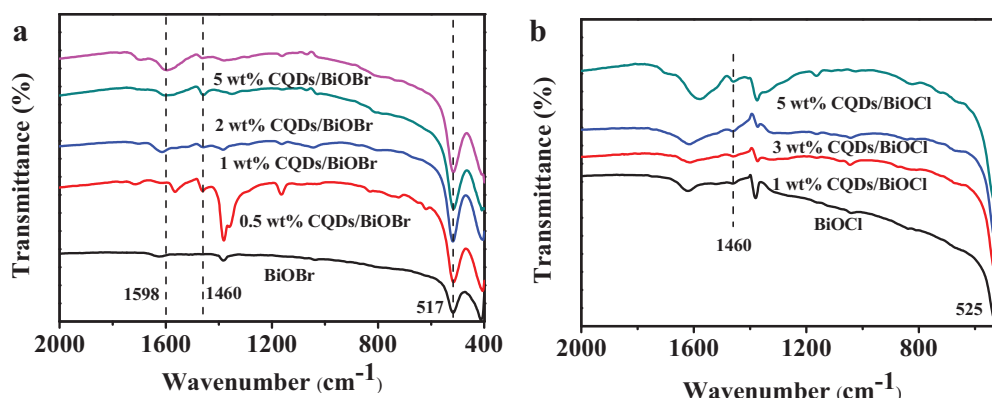


Fig. 4. FT-IR of (a) CQDs/BiOBr and (b) CQDs/BiOCl nanosheets with different contents of CQDs.

carboxyl groups of CQDs. As a result, hydrogen-bond and self-assembly mechanism was helpful to control the growth rate of the certain plane and further allow the crystal to undergo the self-organization into thinner sheet-like structure when appropriate amount of  $[C_{16}mim]Br$  was introduced. The TEM images of CQDs/BiOX nanoplates prepared via NaX were displayed in Fig. S10. As it can be seen, the CQDs cannot distribute uniformly on the surface of BiOX nanoplates and the CQDs amount on the BiOX nanoplates was less than that in CQDs/BiOX nanosheets. The thinner BiOX nanosheets can provide larger surface area to support the CQDs and contact with the contaminants than thicker BiOX nanoplates, which is important for enhancing the photocatalytic activity.

### 3.3. Photocatalytic tests

To compare the photocatalytic activity of CQDs/BiOX composites with different CQDs contents, a series of photodegradation experiments were carried out by using RhB, CIP and BPA as target pollutants under the visible irradiation. Fig. 6a shows the photocatalytic degradation of RhB in the absence or presence of CQDs/BiOBr with different CQDs contents. The results show that the photodegradation rate of RhB is extremely slow when no photocatalyst is added. In the presence of photocatalyst, the CQDs/BiOBr hybrid nanosheets show much higher photocatalytic activity than that of the pure BiOBr nanosheets. Among the different CQDs/BiOBr composite nanosheets, the nanosheets with 3 wt% CQDs loading

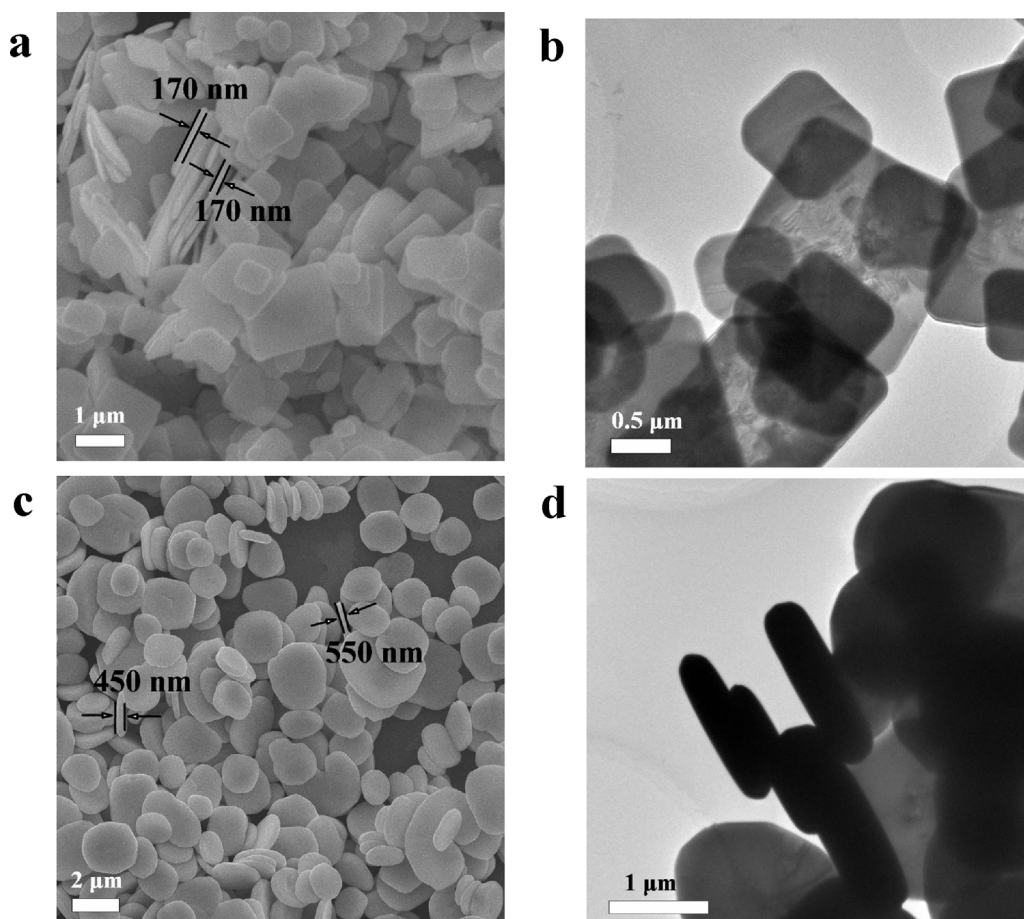
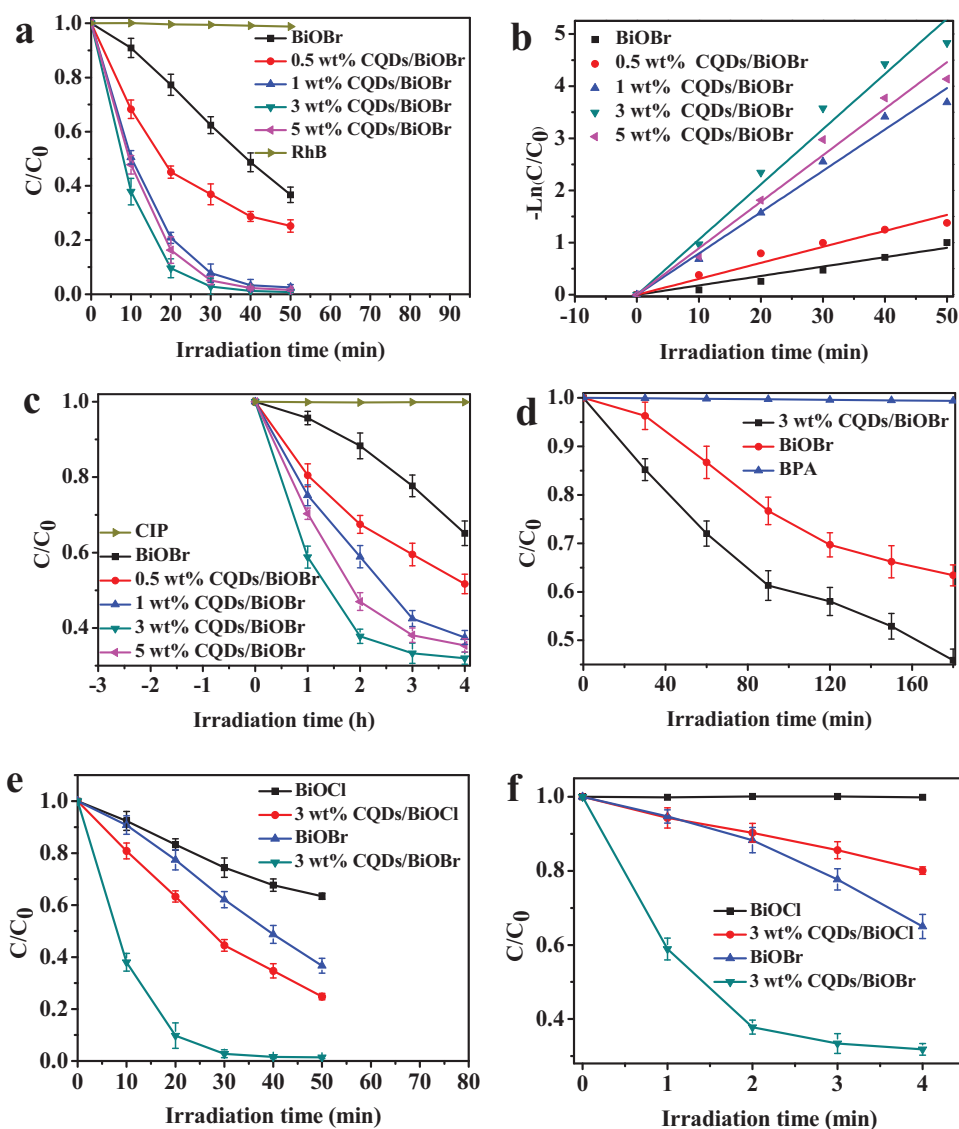


Fig. 5. (a, c) SEM and (b, d) TEM images of (a, b) BiOBr and (c, d) BiOCl nanoplates.



**Fig. 6.** (a) Photocatalytic degradation curves and (b) their Kinetic fit of RhB in the presence of BiOBr and CQDs/BiOBr with different loading amounts under visible light irradiation. Photocatalytic degradation of (c) CIP and (d) BPA in the presence of BiOBr and CQDs/BiOBr nanosheets with different loading amounts under visible light irradiation. The compared photocatalytic activity of BiOBr, BiOCl and 3 wt% CQDs/BiOX nanosheets for the degradation of (e) RhB and (f) CIP.

amount have the highest photocatalytic activity. After the irradiation for 30 min, nearly all of RhB was photodegraded by 3 wt% CQDs/BiOBr composite while only 37% of RhB disappeared by the use of pure BiOBr nanosheets. The photocatalytic degradation kinetics of RhB in the presence of CQDs/BiOBr composites were investigated (Fig. 6b). The apparent rate constant ( $k$ ) of 3 wt% CQDs/BiOBr was  $0.1058 \text{ min}^{-1}$ , which was  $\sim 5.9$  times as high as that of pure BiOBr nanosheets (the pseudo-first-order constants and relative coefficients are summarized in Table S1). When the CQDs loading content is higher than 3 wt%, the composite CQDs/BiOBr nanosheets show a decreased photocatalytic activity for the RhB degradation. The results indicate that the proper introduction of the CQDs is beneficial for the improvement of the photocatalytic performance of CQDs/BiOBr nanosheets.

The present CQDs/BiOX hybrid nanosheet is a general highly efficient photocatalyst for the removal of other pollutants. Ciprofloxacin (CIP), a broad-spectrum antibacterial agent, has been widely used for treating bacterial infections. The presence of CIP in natural environments raises several human health concerns. The toxicity tests reveal that it may cause various adverse effects on

ecosystem by inducing the proliferation of bacterial drug resistance [32]. Therefore, it is significant for the removal of CIP. The as-prepared CQDs/BiOBr was first used to photodegrade the CIP under visible light irradiation, as shown in Fig. 6c. The self-photolytic experiment demonstrates that no CIP is photodegraded by the visible light irradiation. The pure BiOBr nanosheets show poor photocatalytic activity for the degradation of CIP under the same condition, whereas the CQDs/BiOBr composite exhibits the significant photocatalytic activity for the degradation of CIP with 3 wt% CQDs showing the highest photocatalytic activity. These experimental data reveals that the introduction of CQDs favors the enhanced photocatalytic performance for the photodegradation of colorless model organic pollutant CIP. Total organic carbon (TOC) experiment has been carried out for the degradation of CIP by 3 wt% CQDs/BiOBr under visible light irradiation (Fig. S11). After irradiation for 4 h, 44.3% of CIP was mineralized, indicating the CIP can be degraded by CQDs/BiOBr materials under visible light irradiation. Our CQDs/BiOBr hybrid nanosheets show the similar trends on photocatalytic degradation of another pollutant, BPA under visible light irradiation (Fig. 6d). According to the

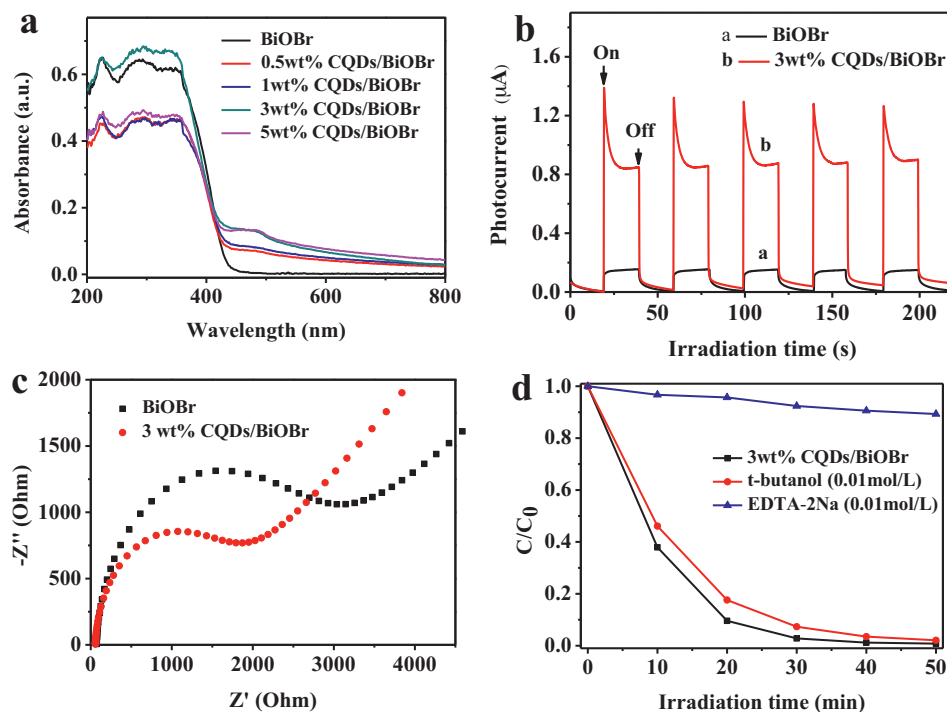


**Fig. 7.** (a) UV-vis diffuse reflectance spectra of the CQDs/BiOBr samples; (b) transient photocurrent response for the pure BiOBr and 3 wt% CQDs/BiOBr composites; (c) Electrochemical impedance spectroscopy of BiOBr and 3 wt% CQDs/BiOBr composite; (d) 3 wt% CQDs/BiOBr composite for the degradation of RhB with or without adding EDTA-2Na and t-butanol under visible light irradiation.

LC-MS analysis (Fig. S12) for BPA degradation, it can be clearly observed that BPA ( $m/z$  227) eluted at a retention time of 5.34 min. Only one intermediate, at  $m/z$  198, was observed by LC-MS analysis at a retention time of approximately 3.65 min, identified as 4-(4-hydroxybenzylidene)cyclohexa-2,5-dienone. The results mean the intermediate [4-(4-hydroxybenzylidene)cyclohexa-2,5-dienone] was produced during the photodegradation reaction and was then degraded continuously during the subsequent photocatalytic process. These photodegradation results of three types of model organic pollutants indicate that the CQDs/BiOBr hybrid nanosheets are very efficient visible-light-driven photocatalyst, making them valuable photocatalytic materials in environmental remediation.

We also compared the photocatalytic activity of BiOBr, BiOCl and 3 wt% CQDs/BiOBr nanosheets for the degradation of RhB and CIP, as shown in Fig. 6e and f. It is obvious that 3 wt% CQDs/BiOBr and BiOBr nanosheets shows better photocatalytic performance than 3 wt% CQDs/BiOCl and BiOCl nanosheets, respectively. Also, through the photocatalytic activity investigation by the degradation of RhB and CIP, it can be found that the CQDs/BiOBr nanosheets prepared by using ionic liquid displayed much higher photocatalytic efficiency than the corresponding CQDs/BiOBr nanosheets prepared by using NaX (Figs. S13–16), further revealing the advantage of ionic liquid in this system. The kinetic fit of RhB in the presence of BiOBr and CQDs/BiOBr reveals that the apparent rate constant of 3 wt% CQDs/BiOBr was almost 2.5 times as high as that of 3 wt% CQDs/BiOCl (The pseudo-first-order constants and relative coefficients are summarized in Table. S1). This is because that the CQDs/BiOBr nanosheets have much better visible light absorption than CQDs/BiOCl nanosheets, as proved by their optical absorption comparison (Fig. S17).

#### 3.4. Structure–activity relationships

There are several important factors that make CQDs/BiOBr hybrid nanosheets be extremely photoactive for the degradation

of organic pollutants. (a) The excellent optical absorption feature of CQDs/BiOBr plays an important role in enhancing its photocatalytic performance. The UV-vis absorption spectra of pure BiOBr and CQDs/BiOBr nanosheets were recorded (Fig. 7a). The BiOBr nanosheets show their fundamental absorption edge rising at 430 nm. With increasing the CQDs content from 0.5 wt% to 5 wt%, the absorption intensity in the range of 430–800 nm of the CQDs/BiOBr nanosheets gradually increases. The UV-vis results suggest that CQDs may play an important role in utilizing sunlight. The enhanced light absorption of CQDs/BiOBr may result in more electron–hole pairs [33]. However, more CQDs on the surface of BiOBr nanosheets will make the BiOBr nanosheets hard to absorb the visible light, leading to lower photocatalytic activity. (b) As is known, the higher the photocurrent is, the better separation efficiency of the electrons and holes will be, and hence a higher photocatalytic activity [34]. The transient photocurrent responses of the as-prepared BiOBr and CQDs/BiOBr modified ITO electrodes were recorded for several on-off cycles under visible light irradiation (Fig. 7b). The photocurrent of the CQDs/BiOBr nanosheets is about 5.8 times as high as that of the BiOBr nanosheets. The enhanced photocurrent of CQDs/BiOBr nanosheets modified electrode indicates the enhanced separation efficiency of photo-induced electrons and holes. (c) Electrochemical impedance spectroscopy (EIS) measurement was used to investigate the interfacial charge transfer resistance of the ITO/BiOBr film and ITO/CQDs/BiOBr film (Fig. 7c). We found that the resistance of ITO/CQDs/BiOBr film is smaller than that of the ITO/BiOBr film, indicating that there exists an effective separation of the photogenerated electrons and holes and a fast interfacial charge transfer after BiOBr nanosheets were hybridized with CQDs [35]. The PL spectrum was performed to further reveal the transfer and recombination process of electron–hole pairs. As shown in Fig. S18, the 3 wt% CQDs/BiOBr materials exhibit lower PL intensity than BiOBr under the excitation wavelength of 360 nm, which indicating the effective separation of photo-generated electrons

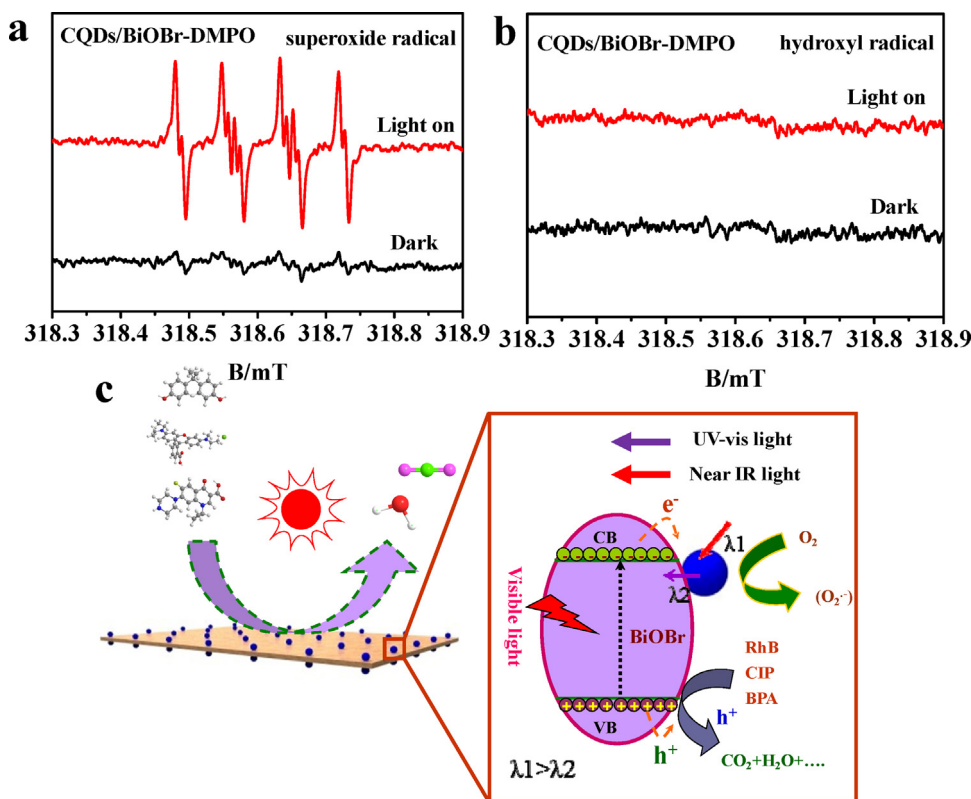


**Fig. 8.** ESR spectra of radical adducts trapped by DMPO in CQDs/BiOBr dispersion in the dark and under visible light irradiation. (a) Superoxide radical; (b) hydroxyl radical; (c) schematic model for the photocatalytic mechanism of CQDs/BiOBr composite nanosheets.

and holes [36]. These results indicate the modification of CQDs could effectively increase the separation efficiency of electron-hole pairs.

### 3.5. Mechanism of pollutant photodegradation

We further explore the photocatalytic mechanism of the prepared CQDs/BiOBr for the degradation of pollutants. Usually, the photogenerated holes and the formed hydroxyl radicals are the two main species for the degradation of organic pollutants. Fig. 7d shows the photocatalytic degradation of RhB in the presence of CQDs/BiOBr nanosheets with the addition of hole and hydroxyl radical scavengers, respectively. Here the addition of tert-butanol (hydroxyl radicals scavenger), just cause a slight decrease of the photocatalytic activity, indicating that a little bit of hydroxyl radicals has been produced during the process of CQDs/BiOBr nanosheets. It is interesting to find that the introduction of EDTA-2Na (capture for holes) can inhibit the RhB photodegradation. These results show that the direct hole oxidation reaction dominates the RhB photodegradation process and the hydroxyl radicals is not the main active species.

In order to deeper understand the photocatalytic mechanism, the ESR spin-trap signals of CQDs/BiOBr nanosheets with DMPO in methanol solution and aqueous solution were investigated, respectively (Fig. 8). Four characteristic peaks of  $\text{DMPO-O}_2^{\cdot-}$  are observed in methanol dispersion of CQDs/BiOBr nanosheets under visible light irradiation (Fig. 8a). Furthermore, no  $\text{DMPO-OH}^{\cdot}$  species are detected in aqueous dispersions of the samples in dark condition and under visible light irradiation (Fig. 8b). These ESR results indicate that the  $\text{O}_2^{\cdot-}$  radical species are produced by the reduction of  $\text{O}_2$  using photo-induced electron in CQDs/BiOBr nanosheets and become the dominant during the photocatalytic process. Therefore, the radicals trap experiments and ESR results reveal that hole and

$\text{O}_2^{\cdot-}$  are the main active species during the photocatalytic process, leading to the improvement of photocatalytic activity. The valence band (VB) of BiOBr materials is measured by using XPS valence spectra, as shown in Fig. S19. The VB maximum of BiOBr was measured to be 2.01 eV. The  $E_g$  is estimated to be 2.77 eV from the onset of the absorption edge in DRS analysis (Fig. S20). The conduction band edge potential ( $E_{CB}$ ) can be acquired by the formula  $E_{CB} = E_{VB} - E_g$ . Thus the  $E_{CB}$  is estimated to be  $-0.76$  eV. Due to the  $E^0(\text{O}_2/\text{O}_2^{\cdot-})$  is about  $-0.046$  eV (vs. NHE) and  $E^0(\cdot\text{OH}/\text{OH}^-)$  is 2.38 eV (vs. NHE), the  $\text{O}_2$  can be reduced to  $\text{O}_2^{\cdot-}$  and  $\cdot\text{OH}$  cannot be generated.

Based on the experimental result in this system and literature references [37,38], the photocatalytic mechanism was proposed. For the CQDs/BiOBr system (Fig. 8c), the electrons can be excited from the VB of BiOBr to the CB when it was irradiated by visible light. Then, the electron could transfer to CQDs and result in efficient separation of electron-hole pairs. On the other hand, the upconverted PL property of CQDs could take the advantage of harnessing the full spectrum of sunlight and in turn excites BiOBr to form electron-hole pairs, therefore improving the photocatalytic activity. With respect to the CQDs/BiOCl system (Fig. S21), due to the BiOCl was a wide band gap semiconductor, it could not be excited by visible light. For the RhB degradation, the RhB dye could absorb the visible light to produce singlet and triplet states (denoted as  $\text{RhB}^*$ ) and the excited electron could inject into the CB of BiOCl. The electron on the CB of BiOCl could migrate to the CQDs and result in effective separation. Then the electron could react with  $\text{O}_2$  to generate  $\text{O}_2^{\cdot-}$  and thus degrade the pollutant effectively. At the same time, the upconverted PL property of CQDs could absorb the long wavelength light and emit shorter wavelength light, and in turn excites BiOCl to form electron-hole pairs. This was the reason that the colorless CIP cannot be degraded by BiOCl but can be partly degraded by CQDs/BiOCl.

#### 4. Conclusion

To summarize, we demonstrate a new ionic liquid-assisted procedure for the controlled synthesis of thin CQDs/BiOX hybrid nanosheets using reactable ionic liquid [C<sub>16</sub>mim]Br and [C<sub>16</sub>mim]Cl as soft template, solvent and dispersing agent. The as-prepared hybrid nanosheets show the interesting CQDs loading content and X composition-dependent photocatalytic activity. 3 wt% CQDs/BiOBr hybrid nanosheets show the optimal visible light-driven photocatalytic activity for the degradation of RhB, CIP and BPA. The results from the optical spectroscopy, photocurrent generation and EIS reveal that enhanced photocatalytic performance of CQDs/BiOBr nanosheets can be attributed to their better optical absorption, higher separation efficiency of the photogenerated electron–holes pairs induced by CQDs and smaller resistance. The radicals trapping experiments and ESR result reveal that hole and O<sub>2</sub><sup>•−</sup> are the main active species during the photocatalytic process, playing the key role in photocatalytic degradation of pollutants. We expect that the strategy developed in this study may open a new way to integrate other interesting visible or infrared responsive QDs with 2D BiOX nanosheets for better photocatalytic degradation or solar fuels production.

#### Acknowledgements

This work was financially supported by the National Nature Science Foundation of China (Nos. 21206060, 21476098 and 21471069), Jiangsu Province (1102118C), and the Special Financial Grant from the China Postdoctoral Science Foundation (2013T60506).

#### Appendix A. Supplementary data

Supplementary data associated with this article can be found, in the online version, at <http://dx.doi.org/10.1016/j.apcatb.2015.07.035>

#### References

- [1] A.K. Geim, I.V. Grigorieva, *Nature* 499 (2013) 419–425.
- [2] C.N.R. Rao, H.S.S.R. Matte, U. Maitra, *Angew. Chem. Int. Ed.* 52 (2013) 13162–13185.
- [3] Y.F. Sun, S. Gao, F.C. Lei, C. Xiao, Y. Xie, *Acc. Chem. Res.* 48 (2015) 3–12.
- [4] H.T. Wang, H.T. Yuan, S.S. Hong, Y.B. Li, Y. Cui, *Chem. Soc. Rev.* 44 (2015) 2664–2680.
- [5] C.L. Tan, H. Zhang, *Chem. Soc. Rev.* 44 (2015) 2713–2731.
- [6] X. Peng, L.L. Peng, C.Z. Wu, Y. Xie, *Chem. Soc. Rev.* 43 (2014) 3303–3323.
- [7] Y.F. Sun, S. Gao, F.C. Lei, Y. Xie, *Chem. Soc. Rev.* 44 (2015) 623–636.
- [8] M.S. Xu, T. Liang, M.M. Shi, H.Z. Chen, *Chem. Rev.* 113 (2013) 3766–3798.
- [9] J. Li, Y. Yu, L.Z. Zhang, *Nanoscale* 6 (2014) 8473–8488.
- [10] J. Di, J.X. Xia, Y.P. Ge, L. Xu, H. Xu, M.Q. He, Q. Zhang, H.M. Li, *J. Mater. Chem. A* 2 (2014) 15864–15874.
- [11] H. Li, J. Shang, Z.H. Ai, L.Z. Zhang, *J. Am. Chem. Soc.* 137 (2015) 6393–6399.
- [12] J. Di, J.X. Xia, S. Yin, H. Xu, L. Xu, Y.G. Xu, M.Q. He, H.M. Li, *J. Mater. Chem. A* 2 (2014) 5340–5351.
- [13] J. Jiang, K. Zhao, X.Y. Xiao, L.Z. Zhang, *J. Am. Chem. Soc.* 134 (2012) 4473–4476.
- [14] K. Zhao, L.Z. Zhang, J.J. Wang, Q.X. Li, W.W. He, J.J. Yin, *J. Am. Chem. Soc.* 135 (2013) 15750–15753.
- [15] J. Di, J.X. Xia, S. Yin, H. Xu, M.Q. He, H.M. Li, L. Xu, Y.P. Jiang, *RSC. Adv.* 3 (2013) 19624–19631.
- [16] D. Liu, W.Q. Yao, J. Wang, Y.F. Liu, M. Zhang, Y.F. Zhu, *Appl. Catal. B* 172 (2015) 100–107.
- [17] K. Li, H.B. Zhang, Y.P. Tang, D.W. Ying, Y.L. Xu, Y.L. Wang, J.P. Jia, *Appl. Catal. B* 164 (2015) 82–91.
- [18] J. Liu, Y. Liu, N.Y. Liu, Y.Z. Han, X. Zhang, H. Huang, Y. Lifshitz, S.T. Lee, J. Zhong, Z.H. Kang, *Science* 347 (2015) 970–973.
- [19] H.T. Li, X.D. He, Z.H. Kang, H. Huang, Y. Liu, J.L. Liu, S.Y. Lian, C.H.A. Tsang, X.B. Yang, S.T. Lee, *Angew. Chem. Int. Ed.* 49 (2010) 4430–4434.
- [20] L. Cao, M.J. Mezzani, S. Sahu, Y.P. Sun, *Acc. Chem. Res.* 46 (2013) 171–180.
- [21] S.Y. Lim, W. Shen, Z.Q. Gao, *Chem. Soc. Rev.* 44 (2015) 362–381.
- [22] Z. Ma, J.H. Yu, S. Dai, *Adv. Mater.* 22 (2010) 261–285.
- [23] M. Smiglak, J.M. Pringle, X. Lu, L. Han, S. Zhang, H. Gao, D.R. MacFarlane, R.D. Rogers, *Chem. Commun.* 50 (2014) 9228–9250.
- [24] M.L. Guan, C. Xiao, J. Zhang, S.J. Fan, R. An, Q.M. Cheng, J.F. Xie, M. Zhou, B.J. Ye, Y. Xie, *J. Am. Chem. Soc.* 135 (2013) 10411–10417.
- [25] J. Di, J.X. Xia, Y.P. Ge, H.P. Li, H.Y. Ji, H. Xu, Q. Zhang, H.M. Li, M.N. Li, *Appl. Catal. B* 168–169 (2015) 51–61.
- [26] X. Zhang, B.H. Li, J.L. Wang, Y. Yuan, Q.J. Zhang, Z.Z. Gao, L.M. Liu, L. Chen, *Phys. Chem. Chem. Phys.* 16 (2014) 25854–25861.
- [27] S.J. Zhu, Q.N. Meng, L. Wang, J.H. Zhang, Y.B. Song, H. Jin, K. Zhang, H.C. Sun, H.Y. Wang, B. Yang, *Angew. Chem. Int. Ed.* 52 (2013) 3953–3957.
- [28] J. Di, J.X. Xia, M.X. Ji, H.P. Li, H. Xu, H.M. Li, R. Chen, *Nanoscale* 7 (2015) 11433–11443.
- [29] J.Z. Li, N.Y. Wang, T.T. Tran, C.A. Huang, L. Chen, L.J. Yuan, L.P. Zhou, R. Shen, Q.Y. Cai, *Analyst* 138 (2013) 2038–2043.
- [30] H.C. Zhang, H. Huang, H. Ming, H.T. Li, L.L. Zhang, Y. Liu, Z.H. Kang, *J. Mater. Chem.* 22 (2012) 10501–10506.
- [31] J.M. Ma, X.D. Liu, J.B. Lian, X.C. Duan, W.J. Zheng, *Cryst. Growth Des.* 10 (2010) 2522–2527.
- [32] T. Paul, P.L. Miller, T.J. Strathmann, *Environ. Sci. Technol.* 41 (2007) 4720–4727.
- [33] J. Di, J.X. Xia, Y.P. Ge, L. Xu, H. Xu, J. Chen, M.Q. He, H.M. Li, *Dalton. Trans.* 43 (2014) 15429–15438.
- [34] M. Zhang, X.J. Bai, D. Liu, J. Wang, Y.F. Zhu, *Appl. Catal. B* 164 (2015) 77–81.
- [35] G.S. Li, B. Jiang, X. Li, Z.C. Lian, S.N. Xiao, J. Zhu, D.Q. Zhang, H.X. Li, *ACS Appl. Mater. Interfaces* 5 (2013) 7190–7197.
- [36] D.Q. Zhang, M.C. Wen, S.S. Zhang, P.J. Liu, W. Zhu, G.S. Li, H.X. Li, *Appl. Catal. B* 147 (2014) 610–616.
- [37] K. Li, Y.P. Tang, Y.L. Xu, Y.L. Wang, Y.N. Huo, H.X. Li, J.P. Jia, *Appl. Catal. B* 140–141 (2013) 179–188.
- [38] H.T. Li, Z.H. Kang, Y. Liu, S.T. Lee, *J. Mater. Chem.* 22 (2012) 24230–24253.